

Impedance Analysis of Silicon Nanowire Lithium Ion Battery Anodes

Riccardo Ruffo,[†] Seung Sae Hong,[‡] Candace K. Chan,[§] Robert A. Huggins,^{||} and Yi Cui^{*||}

Department of Materials Science, University of Milan–Bicocca, Milan, Italy, and Department of Applied Physics, Department of Chemistry, and Department of Materials Science and Engineering, Stanford University, Stanford, California 94305

Received: February 20, 2009; Revised Manuscript Received: April 10, 2009

The impedance behavior of silicon nanowire electrodes has been investigated to understand the electrochemical process kinetics that influences the performance when used as a high-capacity anode in a lithium ion battery. The ac response was measured by using impedance spectroscopy in equilibrium conditions at different lithium compositions and during several cycles of charge and discharge in a half cell vs. metallic lithium. The impedance analysis shows the contribution of both surface resistance and solid state diffusion through the bulk of the nanowires. The surface process is dominated by a solid electrolyte layer (SEI) consisting of an inner, inorganic insoluble part and several organic compounds at the outer interface, as seen by XPS analysis. The surface resistivity, which seems to be correlated with the Coulombic efficiency of the electrode, grows at very high lithium contents due to an increase in the inorganic SEI thickness. We estimate the diffusion coefficient of about 2×10^{-10} cm²/s for lithium diffusion in silicon. A large increase in the electrode impedance was observed at very low lithium compositions, probably due to a different mechanism for lithium diffusion inside the wires. Restricting the discharge voltage to 0.7 V prevents this large impedance and improves the electrode lifetime. Cells cycled between 0.07 and 0.70 V vs. metallic lithium at a current density of 0.84 A/g (C/5) showed good Coulombic efficiency (about 99%) and maintained a capacity of about 2000 mAh/g after 80 cycles.

Introduction

The demand for higher specific energy lithium ion batteries for applications such as electric vehicles, next generation electronic devices, and implantable medical devices motivates the research toward electrode materials with larger specific charge capacities. Among several compounds proposed to replace graphite at the negative electrode, silicon is very promising because it has a theoretical specific capacity of 4200 mAh/g due to the incorporation of 4.4 lithium atoms per one silicon atom.¹ Moreover, since silicon is the second most abundant element on earth and already has a mature industrial infrastructure in existence, it is an attractive material when considering commercial applications. Thus there is a great incentive to find a way to utilize silicon in lithium ion battery systems.

There have been a number of studies on silicon-based electrodes involving submicrometer pillars,² micrometer,³ and nanosized particles,^{4,5} and various composite anodes.⁶ An important feature of all of these silicon-based materials is the large inherent change in specific volume (up to about 410%) during the insertion and extraction of large amounts of silicon.⁷ This causes decrepitation, sometimes called pulverization or crumbling, and a loss of electrical contact between the active material and the current collector. The result is the reduction in the effective capacity during cycling which nowadays has been the main reason preventing commercial application of silicon in lithium ion secondary systems.

Recently, we have developed an electrode platform that uses nanowires (NWs) and core–shell NWs⁸ adhered to the current collector^{9,10} to accommodate the large volume change and to avoid capacity loss during cycling due to the decrepitation. By exploiting the nanometer size in the diameter and keeping free space between NWs, we aim to allow for facile volume expansion while preventing decrepitation. In addition, NWs form direct chemical bonding with the current collector for good adhesion and electron transport, which makes the traditional electrode additives such as the binding polymer and conducting carbon unnecessary. In our previous work^{8–11} we have obtained promising results by using the NW electrode. In fact, by limiting the capacity of the electrode using a lower cutoff potential of 70 mV vs. Li, we observed a specific capacity of about 2800 mAh/g with 85% retention after 50 cycles and more than 99% Coulombic efficiency. Nevertheless, the correlation between structural/morphological features of NWs and their electrochemical performance is still not well understood.

A useful tool to study the electrochemical behavior of electrode materials is impedance spectroscopy (IS). In this experiment, a small sinusoidal voltage stimulus of fixed frequency is applied to an electrochemical cell and its response in terms of current is measured. The ac behavior of an electrochemical system can be investigated by sweeping the frequency over several orders of magnitude (generally from a few mHz to several MHz). In the classical three electrode configuration, the voltage is applied and measured between the working and the reference electrode while the counter electrode collects the induced current. The output impedance is the sum of the impedance due to the working electrode (WE), the interface between the WE and the electrolyte, and the ohmic drop between the WE and the reference electrode (RE). In the case of lithium ion battery components, this approach has been

* To whom correspondence should be addressed. E-mail: yicui@stanford.edu.

[†] Department of Materials Science, University of Milan–Bicocca.

[‡] Department of Applied Physics, Stanford University.

[§] Department of Chemistry, Stanford University.

^{||} Department of Materials Science and Engineering, Stanford University.

widely used and detailed models exist to take into account the different physical, chemical, and electrochemical contributions to the total electrode impedance of the cell or of one single element (positive electrode, negative electrode, or electrolyte) under investigation. The analysis of impedance spectra is usually performed in terms of Nyquist plots where the imaginary part of the impedance is plotted as a function of the real part over a wide range of frequencies. Equivalent circuits built in series or parallel combinations of simple elements like resistance, capacitance, and inductance are often used to qualitatively describe the electrode material, while the determination of their numeric values by fitting procedures yields quantitative data. The kinetic steps common for most lithium ion electrodes have been discussed by Barsoukov.¹² Generally, each process has one characteristic time constant (or a narrow distribution of them) that can be seen by the frequency scan. For example, in the case of carbon anodes, it is possible to describe the total impedance of the electrode as the sum of the resistance and the capacitance of the solid electrolyte interface (SEI) passivating layer, the charge transfer resistance of the intercalation process, the double layer capacitance across the interface, and the solid state diffusion into the center of the active material particle. Other anode materials have been studied through IS, in particular Sn-based compounds, using models similar to those for carbon anodes.¹³ A few reports were also devoted to the investigation of the impedance in silicon systems as carbon-coated microparticles,¹⁴ amorphous thin layers,¹⁵ and 3-dimensional cellular structures.¹⁶

In the present work we describe the impedance behavior of our silicon NW-based electrode at different states of the charge (SOC) or depths of discharge (DOD) and after several charge/discharge cycles in a half cell vs. metallic lithium. We also discuss the contributions of the NW surface resistance and bulk lithium diffusion to the total impedance, as well as the correlation between the impedance response and the behavior under direct current (DC). Finally, we show how the information can be used to improve the electrochemical performance of the electrode.

Experimental Section

Stainless steel (SS) 304 (0.002 in. thick, McMaster-Carr) substrates were covered with Au to serve as the catalyst for SiNW growth. The substrates were heated to 485 °C and 2% silane in Ar was flowed in at 50 sccm with a total chamber pressure of 40 Torr for 20 min. The mass of the SiNWs in a given experiment ($\sim 200 \mu\text{g}/\text{cm}^2$) was accurately determined by using a microbalance (Sartorius SE2, 0.1 μg resolution) to weigh the substrates before and after growth. Most of nanowires have a diameter and length of about 100 nm and 10 μm , respectively. More details about sample preparation can be found in our previous work.^{9,11}

To test the Si NW electrode in lithium ion battery applications, we have used a "coffee bag" cell similar to commercial prototypes. Two and three electrode half-cells were fabricated out of the SiNW/SS working electrode, Li metal foil as both reference and counter electrode (CE), and Celgard 2325 separator soaked in electrolyte. The electrolyte was a commercial solution of 1.0 M LiPF₆ in 1:1 w/w ethylene carbonate:diethyl carbonate (Novolyte). No binders or conducting carbon was used. The cells were assembled inside an Ar-filled glovebox and sealed in aluminized polyethylene laminate bags. Two- and three-electrode half-cells were used in galvanostatic cycling with potential limitation (GCPL) and IS experiments, respectively. Typical SiNW/SS electrode sizes were 1 cm² for GCPL and 4

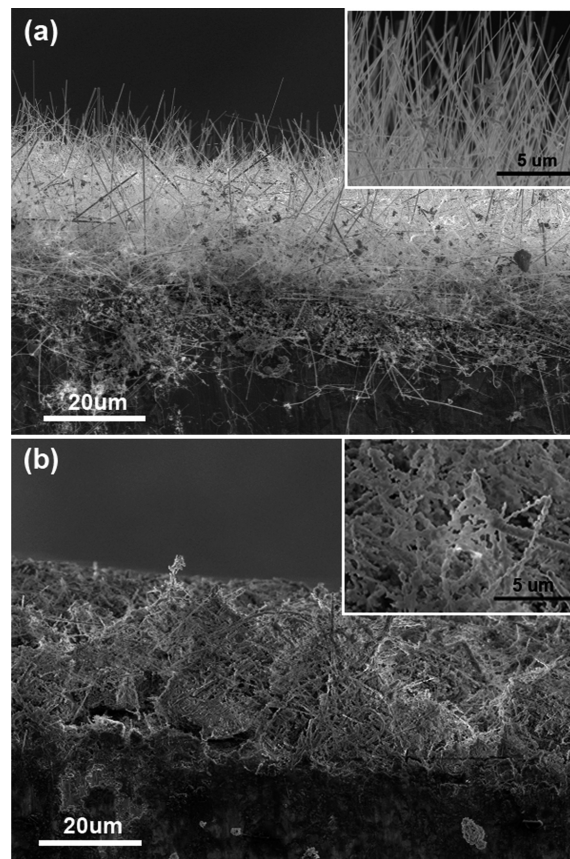


Figure 1. Cross-sectional SEM images of (a) pristine Si NW electrode and (b) of the electrode after the 2nd cycle.

cm² for IS. For impedance measurements several three-electrode cell geometries were tested and evaluated. The explored frequency range was from 50 kHz to 100 mHz under ac stimulus with 10 mV of amplitude and no applied voltage bias. GCPLs were performed at the C/5 rate, using different cutoff voltages. All electrochemical measurements were carried out using a Bio-Logic VMP3 multichannel galvanostat-potentiostat. The impedance data were fitted using the ZSimpWin computer program.

Scanning electron microscopy (SEM) was used to check the electrode morphology before and after the cell assembling. Images were taken with a FEI XL30 Sirion SEM at magnification of 1000 \times .

Several samples were prepared at different SOC and DOD for X-ray photoelectron spectroscopy (XPS) analysis of the surface. After the galvanostatic measurements, the samples were disassembled from the cells and washed in dimethyl carbonate overnight to remove excess electrolyte. The XPS measurements were conducted with a PHI 5000 VersaProbe (Physical Electronics, Chanhassen, MN) equipped with an Al K α X-ray radiation source. The X-ray takeoff angle was 45° and the spot size was about 200 μm . No charge neutralization was used. The survey scans were taken with an energy resolution of 1.5 eV, using a source with power and current of 125 kW and 10 μA , respectively. Survey scans and high-resolution scans of the Si 2p, C 1s, O 1s, F 1s, Li 1s, and P 2p energy spectra were taken of each sample to identify the compounds present on the surface. The high-resolution scans were obtained with a pass energy of 23.5 eV and energy resolution of 0.1 eV. The spectra were calibrated to the hydrocarbon peak at 284.5 eV. The molecular composition of the SEI layer was determined by analyzing the

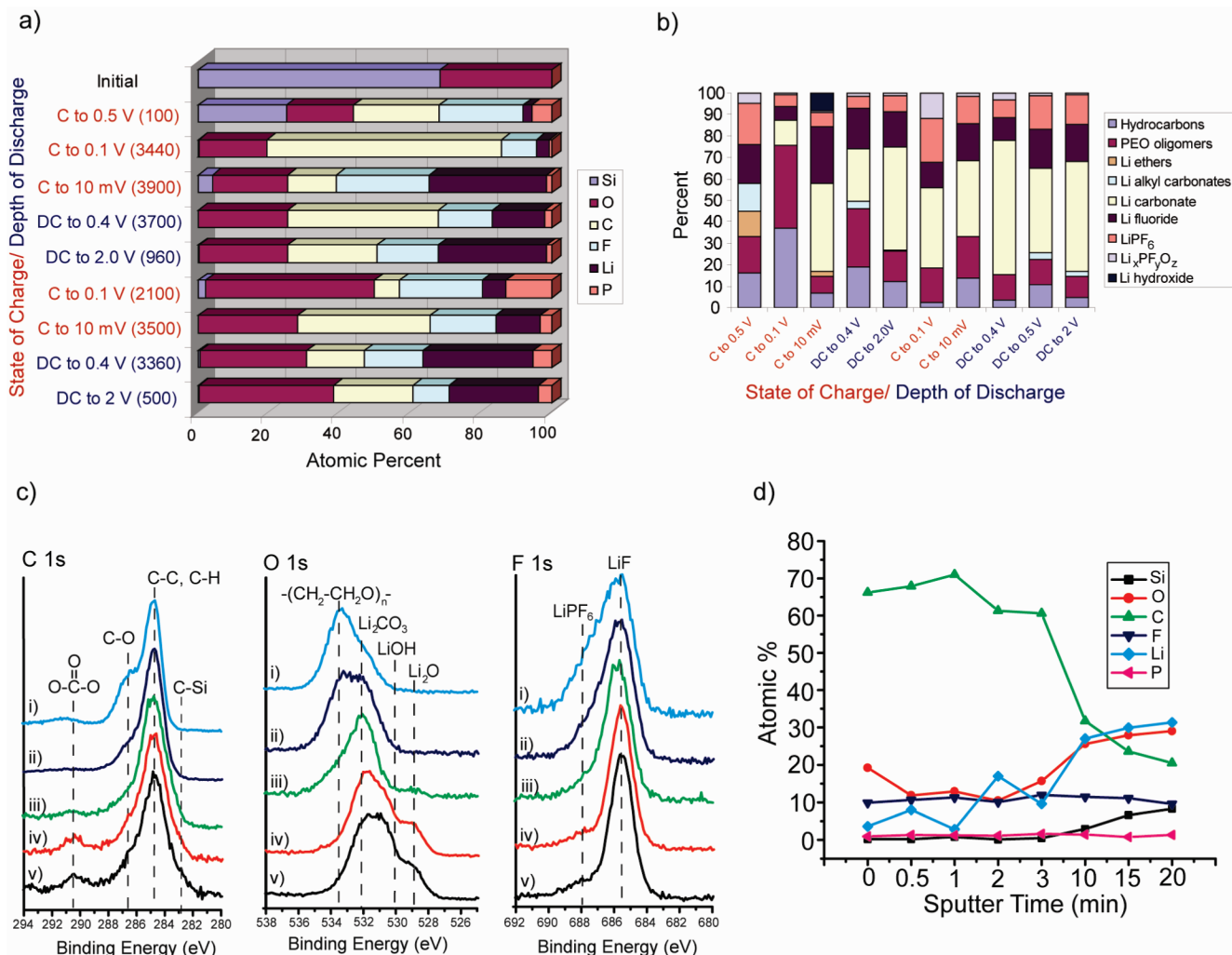


Figure 2. (a) Atomic composition of the SiNW surface determined by XPS survey scan at different SOC and DOD (capacity in mAh/g shown in parentheses). (b) Molecular composition of the SiNW surface determined by XPS high-resolution analysis (same capacities as in panel a). (c) High-resolution spectra for the C 1s, O 1s, and F 1s peaks for the SiNW sample charged to 0.1 V shown after different sputtering times. Using an approximate sputter rate of 4 nm/min, the thicknesses are (i) 0 (initial surface prior to sputtering), (ii) 2, (iii) 12, (iv) 60, and (v) 80 nm. (d) The depth profile from the SiNW sample charged to 0.1 V with an approximate sputter rate of 4 nm/min.

XPS high-resolution scans. For more information on the peak assignments, see ref 11.

Results and Discussion

Electrode Morphology. As shown in Figure 1a, the electrode consists of a high density of NWs attached to the substrate. The electrode is in mechanical contact with the separator, which is soaked with the electrolyte. When the cell is assembled, a slight amount of pressure is applied to the cell, which causes the NWs to lie down mostly parallel to the substrate. As shown in Figure 1b, which was obtained by disassembling the cell after the charge, the electrode appears as a dense mass of wires packed together between the separator (not shown) and the substrate.

XPS Analysis. XPS data reported in Figure 2 show the composition of the wire surface at different capacities. As we can observe, the distribution of the elements (Figure 2a) varies for each sample, suggesting that the surface composition is dominated by the SEI layer formation, which is a dynamic process over the voltage range used. The signal from the Si disappears at 0.1 V in the first charge, indicating that the SEI layer has grown thicker than the XPS penetration depth (~10 nm). Figure 2b shows a summary of the composition of the

surface of each sample as determined by identifying the compounds from the high-resolution spectra (data for charge to 0.1 V are shown in Figure 2c). At the first charge to 0.5 V, the SEI layer is composed of hydrocarbons, PEO-type oligomers, and lithium salts (LiF and LiPF₆), with smaller amounts of ethers and lithium alkyl carbonates. The observed species are consistent with previously reported studies about reduction products observed in this electrolyte.¹⁷ In the first charge to 0.1 V, the SEI surface consists mainly of hydrocarbons and PEO-oligomers, indicating further electrolyte reduction; no Li alkyl carbonates or ethers were observed, suggesting that these products transformed into Li₂CO₃. Upon sputtering (Figure 2d), C–O features were observed to disappear from the C1s peak, indicating that hydrocarbons and PEO are part of an organic layer on the surface. LiPF₆ species were also found on the outer layer, with more LiF inside on the surface of the electrode. This is consistent with previous observations on Li and Li_xC electrodes, where the SEI consists of an inorganic layer closer to the surface of the electrode and an organic, polymer-containing layer at the interface with the electrolyte. At the full charge to 10 mV, the SEI surface contains mainly Li₂CO₃ and LiF. The Li₂CO₃ is formed as a product of electrochemical reduction of the electrolyte, but the LiF is formed as a

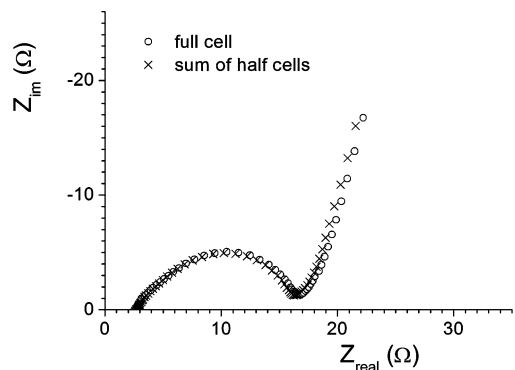


Figure 3. Comparison between the impedance response obtained in a two-electrode condition and the sum of the two three-electrode configurations.

decomposition product (of LiPF_6) rather than an electrochemical one. The SEI layers at 0.4 V in the dealloying (discharge) have again LiF and Li_2CO_3 as major components. At the full discharge to 2 V, the SEI was found to be composed predominantly of Li_2CO_3 , with other major species being LiF and LiPF_6 . During the second cycle, the composition remains the same during both the charge and discharge. This suggests that the compositional formation of the SEI is an important feature during the first cycle and afterward stays mostly the same, with Li_2CO_3 as the major species.

IS Data Validation. The geometry used in the impedance experiment was chosen and validated by using two three-electrode configurations where the impedances of the WE vs. the RE and that of the CE vs. the RE were measured. If the measurement is independent of the shape and position of the RE, the sum of those two impedances has to be similar to that obtained in a two-electrode configuration between the WE and the CE.¹⁸ In our case, the best result was obtained by placing a small Li RE (about 6 mm²) between two separator sheets in the middle of a pouch cell. The RE is connected to the outside of the cell through a polyimide-insulated copper wire.¹⁹ Using this geometry, the sum of the WE/RE and CE/RE impedances differed from that of the WE/CE impedance by less than 6% in the explored frequency range. The comparison between the sum of the two half cells' value and the full cell's value is reported in Figure 3. Stable, reproducible spectra can be obtained by using this geometry at frequencies higher than 100 mHz.

IS Experimental Sequence. The change in composition of the SiNW electrode is described in terms of the state of charge (SOC) during lithium insertion and depth of discharge (DOD) during lithium extraction. To change the SOC and DOD, we used galvanostatic pulses (0.21 A/g) during the first two charge and discharge cycles. The cell was then cycled by GCPL at 0.42 A/g for an additional 8 cycles (during cycles 3–10). At the eleventh and twelfth cycles impedance measurements were taken again at different SOC and DOD. After the twelfth cycle the cell was opened and all of the components (CE, RE, separator sheets, and electrolyte) except for the WE were substituted with new ones. IS measurements were carried out again for the thirteenth cycle. Each IS spectrum was collected at the end of the corresponding galvanostatic step after waiting a certain amount of time for relaxation at the open circuit voltage condition (OCV). The OCV potential drift (measured as mV/h) is an important parameter in defining the equilibrium conditions attained from the electrode, and it has great influence on the linearity of IS measurements. After 15 h of relaxation, the slope of the curve OCV/time is usually less than 0.5 mV/h; only at deep discharge states did we observe a bigger and

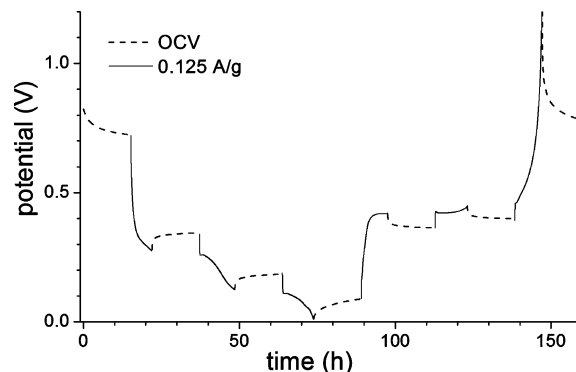


Figure 4. Voltage/time profile under constant current (continuous line) and relaxation (dashed line) conditions. IS experiments were performed at the end of each relaxation.

constant value up to 1.0 mV/h. However, no substantial drift was observed in spectra collected at different times in the explored frequency range. A typical voltage time profile is shown in Figure 4. The profile itself is a galvanostatic intermittent titration curve (GITT) with long current pulses which can be employed to monitor the evolution of the internal resistance. The internal resistance can be evaluated from the difference in potential at the end of the current step and at the end of the relaxation³ on the current impulse. Panels a and b of Figure 5 show the OCV and the cutoff voltage of each step as a function of the capacity for the first and the second cycles. The corresponding internal resistance values, reported in Figure 5c for the first and the second cycles, are around 1000 Ω at high SOC, then decrease to 600–700 Ω in the middle of the discharge, and then increase 1 order of magnitude at high DOD.

Equivalent Circuit. The electrode morphology described in Figure 1b is similar to a thin film of mixed ionic/electronic conductor with a large surface area and pores that can be partially filled by the liquid electrolyte. Part of the external surface of each NW is in contact with the electrolyte and may be covered with SEI, while other parts may be in contact with other NWs also covered with SEI. The base of each NW is also in contact with the current collector. In such a system, either charge transfer or solid state diffusion is usually limiting the kinetics of guest ion insertion or deinsertion processes for lithium inside the Si structure. Several equivalent circuits can be used to describe the situation, from the simple Randles-type circuit to more complex systems built by several subcircuits. The ambiguous situation is also complicated by the fact that several equivalent circuits have the same mathematic representation. However, the impedance of lithium ion battery electrodes is usually modeled by considering all the processes in series with each other, with each chemical-physical process represented by a subcircuit element.¹² In our case, the electric equivalent circuit is given in Figure 6, where R_{ser} is the uncompensated ohmic resistance of the electrolyte, Q_{dl} is the double layer pseudocapacitance of the NW/electrolyte interface, R_{sur} is the resistance of the NW surface (charge transfer between the solid electrolyte layer and the NW), and Z_{d} represents the impedance element describing the solid state diffusion process inside the NWs.

Analysis of Nyquist Plots. The impedance features can be discussed in terms of Nyquist plots for analyzing the different contributions to the total electrode impedance. Typical Nyquist plots of Si NWs are reported in Figure 7, panels a and b, obtained at high SOC and DOD, respectively. The solid lines in the figure are the results of the fitting procedure using the equivalent circuit in Figure 6.

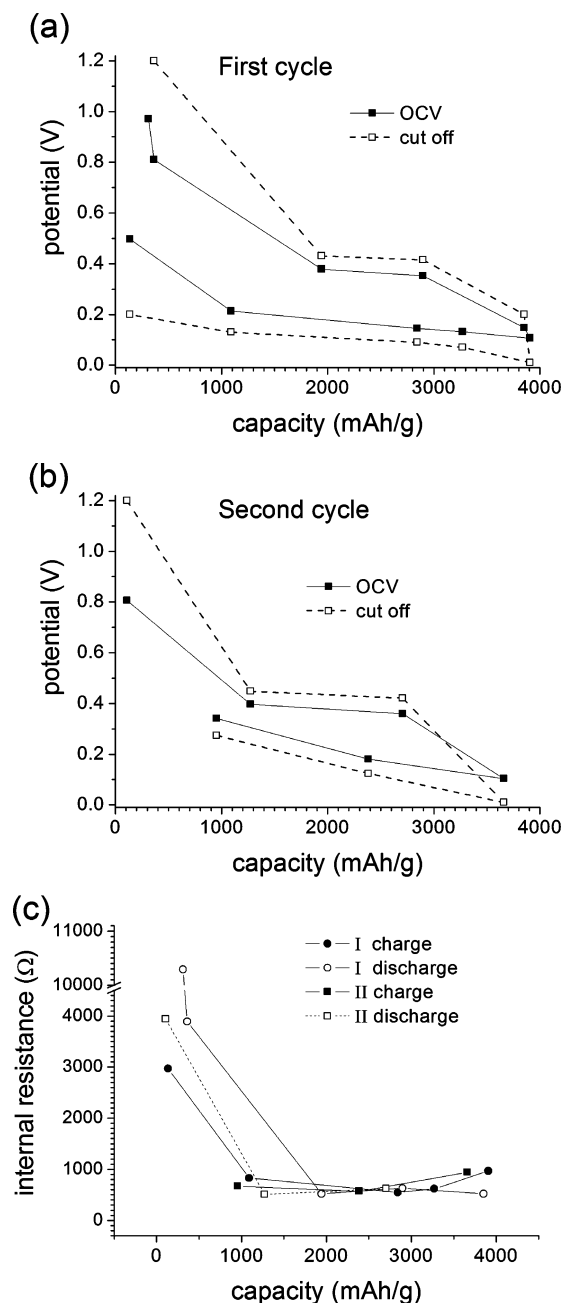


Figure 5. OCV and cutoff potentials from the (a) first and the (b) second cycles. (c) Corresponding internal resistance calculated from the potential difference on the current.

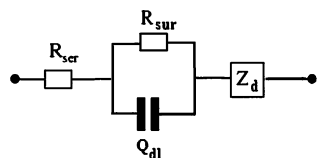


Figure 6. Equivalent circuit used to fit impedance data. R_{ser} and R_{sur} are the serial and surface resistance, respectively, Q_{dl} is the double layer pseudocapacity, and Z_d is the diffusion element.

At high frequencies (above 10 kHz), the spectrum is dominated by the contribution of the external cell connections, the electronic conduction between the substrate and the active material (in our case, likely an ohmic contact due to iron silicide formation at the SiNW-SS interface⁹), and the ionic conduction through the electrolyte. Since the highest experimental frequency is too low to see inductance distortion in the spectra, these

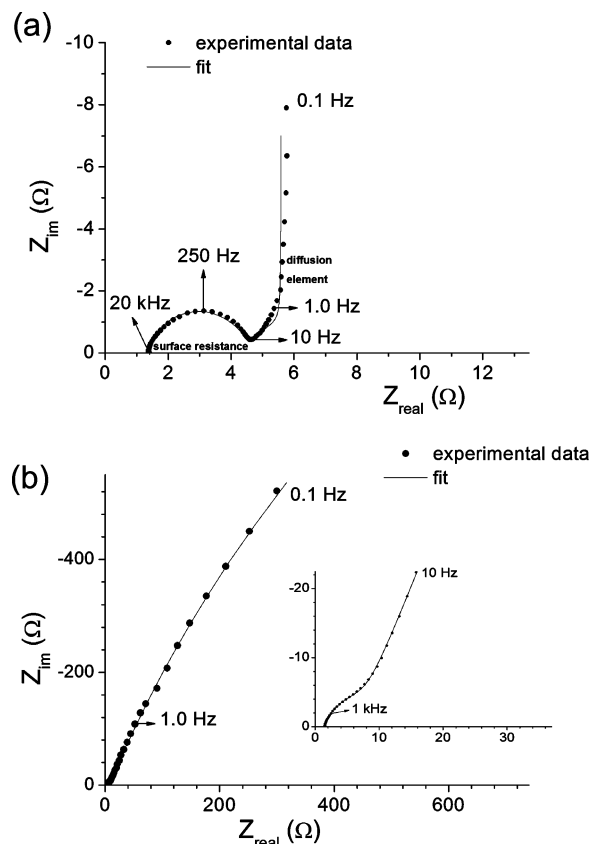


Figure 7. Typical Nyquist plot showing the experimental data at (a) intermediate and high capacity and (b) a very high depth of discharge (less than 500 mAh/g of charge remaining).

contributions appear as a pure resistive behavior (Z_{im} close to 0) and are dominated by the ionic conductivity of the electrolyte. This can be determined by the high-frequency intercept of the real axis (points around 15–20 kHz). No significant changes were observed in R_{ser} (about 1.5 Ω) throughout all the experiments and also after the cell disassembling and reassembling.

As the frequency decreases (between 10 kHz and 10 Hz) each active component (NW) of the electrode contributes to the surface resistance, which is due to the active electron transfer resistance on the electrode interface and the presence of a passivating SEI layer. This resistive contribution is in parallel with the double layer capacitance and appears in the Nyquist plot as a depressed semicircle having a diameter equal to the value of the surface resistance. In our model in Figure 6, the double layer capacitance has been replaced by the constant phase element Q because the NW size is not constant and their diameter and length are distributed around average values.⁹ The determination of the surface resistance can be made by fitting procedures using the equivalent circuit in Figure 6 or directly from the semicircle diameter in the Nyquist plot. The former approach has the advantage that the errors in the parameter have electrical units allowing us to evaluate their significance. In our model the determination of the surface resistance has a numerical error that is usually lower than 1%.

At lower frequencies (below 10 Hz), the contribution from solid state diffusion is present, i.e., Li ions moving into the bulk of SiNW active material. In this frequency region the spectrum (Figure 7a) shows a clear semi-infinite diffusion element due to the presence of the metallic current collector interface, which blocks the diffusion of ions (SS does not alloy with Li). In this

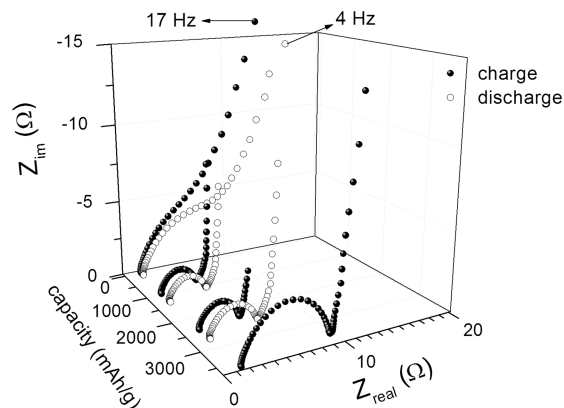


Figure 8. Nyquist plot at different capacities measured for the second charge/discharge cycle.

case, the Z_d element in the equivalent circuit in Figure 6 corresponds to a tangent-hyperbolic function (T) widely discussed in the literature^{20–22} that has admittance ($Y = Z^{-1}$) mathematic representation equal to

$$T = Y^*(\omega) = Y_0 \sqrt{j\omega} \tanh[B\sqrt{j\omega}]$$

where $j = \sqrt{-1}$, ω is the applied frequency, Y_0 is the preexponential factor, and B is a parameter that depends on the electrode geometry, the electrochemical properties of the active material, and the diffusion coefficient of the guest ion in the host structure. The representation of T in the Nyquist plot is a diffusive Warburg segment at 45° followed, at lower frequencies, by a vertical capacitive line. The diffusion process can be characterized by a limiting capacity (C_d) and a diffusion resistance (R_d). C_d is the capacity corresponding to the vertical low-frequency line in the Nyquist plot ($C_d = -1/\omega Z_{im}$), while R_d is the portion of the real axis between the high-frequency tail of the surface semicircle and the projection of the vertical capacitive line. C_d and R_d can be obtained directly from the IS spectra or by spectrum fitting through the tangent hyperbolic element $T = Y^*(\omega)$ containing B and Y_0 variable parameters, which can be combined as $R_d = B/3Y_0$ and $C_d = Y_0B$.²² Since we do not have a thin film but rather an ensemble of NWs, it may not appear straightforward to use these relationships. However, because the NW density is high and the NWs tend to lie down almost parallel to the current collector (Figure 1b), they form a “pseudofilm”.

Except for impedance spectra obtained at very high DOD (measured usually at the end of the discharge), those measured at different SOC, DOD, or cycle number have generally the same features of that reported in Figure 7a. Nyquist plots for the second cycle at different SOC, either during charge or discharge, are reported in Figure 8 wherein they are plotted from 0.1 to 50 kHz, while the two spectra at very high DOD, which are similar to the spectrum in Figure 7b, are cut at about 10 Hz. In the latter case the low-frequency diffusive process appears as a portion of an arc that has a time constant 1 order of magnitude less than that of the surface process. The two elements are partially overlapped (see the inset of Figure 7b) and the deconvolution can be performed by using a RQ parallel element in the Z_d subcircuit in Figure 6. The introduction of the resistance element (called R_{np}) is justified by the net decrease in the statistical error parameter during the fitting procedure (the χ^2 is about 1 order of magnitude lower). The measured resistance R_{np} , listed in Table 1, is 3 orders of magnitude greater

TABLE 1: Low-Frequency Impedance Fitting Parameters of High DOD Data^a

cycle	capacity (mAh/g)	R_{np} (k Ω)	$Y_0(\Omega^{-1}s^n) \times 10^3$	n
1	360	2.2 ± 0.4	5.6	0.72
1	310	4.4 ± 0.6	2.1	0.75
2	110	2.1 ± 0.4	5.6	0.72
11	0 (charge)	0.9 ± 0.1	3.8	0.80
11	70 (discharge)	1.0 ± 0.1	9.0	0.76
13	650	2.3 ± 0.2	5.6	0.85

^a Results for Z_d fit by using $R_{np}Q_d$ subcircuit. Y_0 and n are the two elements used to fit the constant phase element Q .

than R_{sur} or R_d resulting in a dramatic increase in the overall electrode impedance. The origin of this increase as well as the physical meaning of the new subcircuit is still unclear. The XPS analysis discussed previously does not support surface modification that can justify the contribution due to a new interface resistance at high DOD. In fact, at very high DOD the surface composition turns out to be almost the same and is dominated by the presence of inorganic species close to the NW surface. Perhaps the new subcircuit describes a different diffusion mechanism with a possible additional contribution due to a phase change in the NW.¹² The constant phase element is frequently used in solid state electrochemistry and already has been used to model diffusion.¹⁹ It is also possible that the diffusive process deviates from the usual relationship due to the kinetics of structural changes,¹² even if these effects are usually seen at much lower frequencies (few mHz). Another possible explanation is that, due to the morphology changes during cycling of the NWs at very deep states of discharge, the electrode morphology changes from a “quasi”dense to a highly porous film, altering the diffusion process that can no longer be described by the “pseudo”thin film model. A partial dissolution of the SEI at very high potentials, as observed with scanning electron microscopy,¹¹ supports the concept of this porous film. This porous film would have a dramatic change in the diffusion mechanism as well as impedance treatment compared to the other model.

Analysis of the Surface Resistance. The surface resistance can be analyzed regarding its variation with Li concentration (SOC or DOD) during one cycle or at fixed SOC among different cycles (Figure 9). In Figure 9a, obtained during the second cycle, the surface resistance shows a minimum for intermediate SOC around 1000 mAh/g. The slight increase at high SOC is in agreement with that already observed in the literature for amorphous silicon thin films and has been attributed to the growth in thickness of the SEI when the potential becomes more negative.¹⁵ XPS analysis with surface sputtering suggests that the growth in thickness (and in impedance) is due to the inorganic components of the SEI. The surface resistance increase at high DOD is probably the effect of the porous formation on the SEI surface or its dissolution, indicating that the passivating layer is not really homogeneous at low lithium composition.

The change in surface resistance during cycling at the same SOC (around 900 mAh/g) is reported in Figure 9b. Between the first and the second cycle, the surface resistance decreases substantially and after 10 cycles becomes 1 order of magnitude less. No relevant differences were observed between the spectra corresponding to the eleventh and twelfth cycle. However, once the cell was opened and both separator and electrolyte were replaced with fresh ones, the resistance reverted back to the first cycle value and started to decrease in the next cycle. It is important to point out that the sample was kept wet with electrolyte solution during the time the cell was rebuilt in the

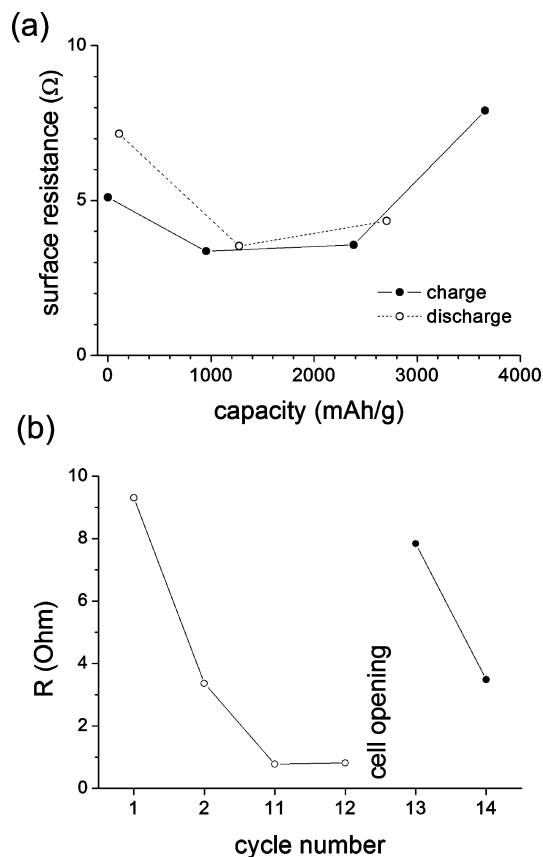


Figure 9. (a) Surface resistance trends vs. capacity for the second cycle and (b) vs. cycle number for the charge state of about 900 mAh/g.

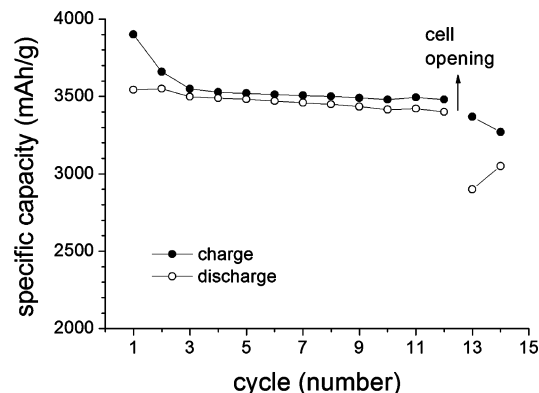


Figure 10. Specific capacity of charge/discharge cycling as measured during both IS and GCPL three-electrode experiments.

glovebox. Thus, we do not believe the procedure alters the “internal” interface between the Si and the SEI, which is made from insoluble inorganic lithium salt (LiF and Li_2CO_3) as confirmed by XPS analysis. It seems that during the first few cycles the surface resistance depends mainly on the external organic SEI/liquid electrolyte interface and in minor part on the charge transfer across the NW/SEI interface. Several charge/discharge cycles are necessary to fix the external interface which was destroyed during the replacement operation. An interesting observation is that the Coulombic efficiency of the 13th cycle decreased to a value similar to that obtained at the end of the first discharge. The external interface has to be “rebuilt” during the first cycle in the fresh electrolyte. Figure 10 shows the charge and discharge specific capacity of the SS/SNWs electrode as a function of the cycle number. The efficiency increases during the first three cycles from about 90% to 99% and then slightly

TABLE 2: Calculated Diffusion Coefficients^a

cycle	capacity (mAh/g)	D (cm^2/s) $\pm 0.5 \times 10^{10}$
1	1090 (charge)	2.0
1	2900 (discharge)	2.0
2	2385 (charge)	2.0
2	1275 (discharge)	1.5
11	840 (charge)	3.0
11	3495 (charge)	1.5
11	1155 (discharge)	3.0
13	1920 (discharge)	2.0

^a The diffusion coefficient was calculated for several capacities fitting Z_d with the hyperbolic tangent T element.

decreases until the cell is disassembled. At the 13th cycle it drops to 85% and starts growing again. The analogy with the decreasing trend in surface resistance is straightforward and the two parameters appear to be directly correlated.

Analysis of the Diffusion Process. From the low-frequency capacity C_d and the diffusion resistance R_d , it is possible to calculate the diffusion coefficient of the lithium ions in the NW. In fact, it is possible to demonstrate that the diffusion coefficient can be obtained as $D = L^2/(3C_dR_d)$, where C_d and R_d are the capacitive and the resistive limiting diffusion values and L is the thickness of the film.²⁰ In our “pseudofilm” model, D is an “effective” diffusion coefficient that describes the diffusion of the lithium ions from the surface of the fraction of the NW surface exposed to the liquid interface toward the current collector or to the complex NW/SEI interphase of another wire. The case would be different, for example, in a beaker cell wherein each NW would be completely surrounded by liquid electrolyte and D represents the diffusion coefficient from the external surface area to the center of the wire. The SEM images in Figure 1b provide support that this picture fits the electrode morphology. However, the results of the error analysis in the fitting procedure point out that the C_d and R_d values from the spectra should be considered only an approximate method to estimate the diffusion coefficient. The situation is even more complicated because the NWs change in volume during the electrochemical process. In fact, high-resolution SEM analysis showed that the diameter increases from about 100 to 150 nm at the end of the charge.⁹ Under these basic assumptions, we have obtained several D values at different SOC and DOD during cycling with the best fitting procedures (Table 2). The lithium diffusion coefficient in silicon electrodes has been reported in ref 14 for a conventional powder electrode. Compared to data in the literature (1.7 and 6.4×10^{-11} cm^2/s for 800 and 1200 mAh/g SOC, respectively), our diffusion coefficient is 1 order of magnitude larger.

Comparison between ac and dc Behavior. A direct comparison between the ac and dc response of the cell can be performed by considering the internal resistance values (Figure 5c,d) and the total ac resistance measured by the impedance response (the limit of the real part of the complex impedance function when the frequency approaches 0). In the equivalent circuit in Figure 6, when Z_d is the tangent-hyperbolic function, the limit is due to the sum of R_{ser} , R_{sur} , and R_d ; otherwise (when the diffusion element is modeled by the RQ subcircuit at high DOD) it is the sum of R_{ser} , R_{sur} , and R_{np} . If all the kinetic processes responsible for the electrode behavior are present in the explored frequency range, the total ac resistance of the electrode should be equivalent to the internal dc resistance.

When Z_d is modeled by the hyperbolic tangent element (T) (as in Figure 7a) it is evident that the total ac resistance is 2

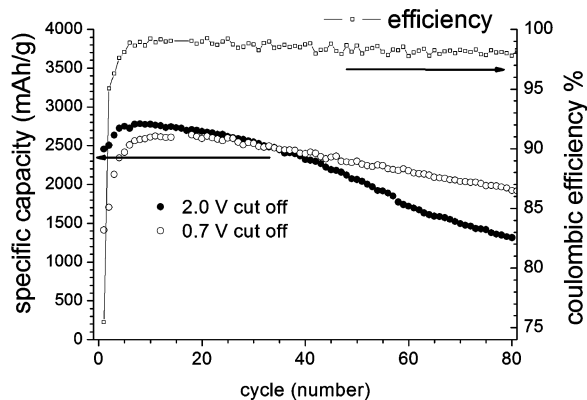


Figure 11. Galvanostatic cycling results of the two-electrode half cell cycled between different cutoff potentials. Coulombic efficiency is reported for the 0.07–0.70 voltage range.

orders of magnitude lower than the dc internal resistance of the system. In other words, from the impedance analysis, we expect a drop in potential of a few millivolts rather than several hundreds of millivolts (from Figure 5a,b) after the current is switched off. To explain the discrepancy we have to consider that the explored frequency range in our experiment is usually too high to see modifications which have very long kinetics. In fact, the voltage time profile in Figure 2 is characterized by a sudden drop followed by a slow relaxation of the potential. We have considered the system in equilibrium when the OCV/time slope is lower than 0.5 mV/h (usually is less than 0.3 mV/h) but we are probably in a metastable condition that evolves with time. Due to the very slow kinetics, the processes (usually due to structural modification¹²) can be seen in impedance spectroscopy only at a much lower frequency.

When the diffusion element is modeled by the $R_{np}Q_d$ subcircuit (at high DOD, as in Figure 7b), the sum of the impedance resistance becomes comparable to the internal resistance. We also observed the OCV/time slope is about 1 mV/h. At this DOD, the processes responsible for the slow relaxation time become faster, can be found at higher frequencies, and could be connected to the R_{np} value introduced in the model.

Galvanostatic Continuous Cycling. In our previous work,¹¹ we have observed better performance when the SiNWs are cycled between 0.07 and 2.0 V instead of 0.01 and 2.0 V vs. metallic lithium; in fact, both the Coulombic efficiency and the capacity retention are higher in the smaller potential range. In the present work we have shown that at high SOC the surface impedance is greater than at intermediate charge states. We have also found a correlation between the Coulombic efficiency and the surface resistance. Moreover, since the impedance increases dramatically at a very high DOD, galvanostatic cycling has been performed by using a lower discharge cutoff potential with a current of 0.84 A/g (C/5). To lower the impedance without reducing too much reversible capacity, we cycled a two-electrode half cell in the potential range between 0.07 and 0.70 V by GCPL. The corresponding results are reported in Figure 11 in terms of specific capacity and coulomb efficiency and compared, over 80 cycles, with the values from the cycling between 0.07 and 2.0 V.

The initial specific capacity of the electrode is 1400 mAh/g with a Coulombic efficiency of 75% in the first cycle. During the first 14 cycles, the capacity and the efficiency increased to 2600 mAh/g and 99.2%, respectively. The cell cycled with the higher discharge cutoff potential (2 V) shows higher capacities for the first 40 cycles, but afterward the performance became

worse. With the optimized voltage range (0.07–0.70 V), the cell shows a capacity retention after 80 cycles higher than 100% and 70% with respect to the first and the tenth cycle (having the greatest capacity); moreover, the Coulombic efficiency is about 99% during all cycles.

Conclusion

We have already demonstrated that the SiNW-based electrode shows promising performance when cycled in a half cell prototype vs. metallic lithium. Our chemical and electrical analysis shows that the SEI formation is a potential dependent process and that achievement of a compact layer is a crucial requirement for optimizing the charge/discharge efficiency. However, IS alone cannot be used to describe the electrode kinetics because we should use much lower frequencies to monitor the very slow processes responsible for the electrode equilibration at OCV. We have to point out that these frequencies could be reached with normal experimental setups, but are not compatible with conditions required to have very stable measurements.

At low lithium compositions in the silicon NWs (high DOD), an abrupt increase in the electrode impedance was observed in both the ac and dc responses. The reasons for this increase are still not well understood and may be due to structural transformations which have slow kinetics. The attempt to limit the impedance growth by changing to the cycled potential range found that between 0.07 and 0.70 V the electrode is able to deliver 2000 mAh/g after 80 cycles with good efficiency and a capacity retention.

Acknowledgment. Y.C. acknowledges support from the Global Climate and Energy Project at Stanford, U.S. Office of Naval Research, and King Abdullah University of Science and Technology. C.K.C. acknowledges support from a National Science Foundation graduate fellowship and Stanford Graduate Fellowship.

References and Notes

- Wen, C. J.; Huggins, R. A. *J. Solid State Chem.* **1981**, *37*, 271.
- Green, M.; Fielder, E.; Scrosati, B.; Wachtler, M.; Moreno, J. S. *Electrochem. Solid-State Lett.* **2003**, *6*, A75–A79.
- Ryu, J. H.; Kim, J. W.; Sung, Y.-E.; Oh, S. M. *Electrochem. Solid-State Lett.* **2004**, *7*, A306–A309.
- Li, H.; Huang, X.; Chen, L.; Wu, Z.; Liang, Y. *Electrochem. Solid-State Lett.* **1999**, *2*, 547–549.
- Graetz, J.; Ahn, C. C.; Yazami, R.; Fultz, B. *Electrochem. Solid-State Lett.* **2003**, *6*, A194–A197.
- Kasavajjula, U.; Wang, C.; Appleby, A. J.; Power, J. *Sources* **2007**, *163*, 1003–1039.
- Boukamp, B. A.; Lesh, G. C.; Huggins, R. A. *J. Electrochem. Soc.* **1981**, *128*, 725–729.
- Cui, L.-F.; Ruffo, R.; Chan, C. K.; Peng, H.; Cui, Y. *Nano Lett.* **2009**, *9* (1), 491–495.
- Chan, C. K.; Peng, H.; Liu, G.; McIlwrath, K.; Zhang, X. F.; Cui, Y. *Nat. Nanotechnol.* **2008**, *3*, 31–35.
- Chan, C. K.; Zhang, X. F.; Cui, Y. *Nano Lett.* **2008**, *8*, 307–309.
- Chan, C. K.; Ruffo, R.; Hong, S. S.; Huggins, R. A.; Cui, Y. *J. Power Sources* **2009**, 1132–1140.
- Barsoukov, E. In *Impedance Spectroscopy: Theory, Experiment, and Applications*; Barsoukov, E., Macdonald, J. R., Eds.; John Wiley and Sons, Inc.: Hoboken, NJ, 2005; pp 444–457 and 462–468.
- Li, H.; Huang, X.; Chen, L.; Power, J. *Sources* **1999**, *81*–82, 340–345.
- Dimov, N.; Fukuda, K.; Umeno, T.; Kugino, S.; Yoshio, M. *J. Power Sources* **2003**, *114*, 88–95.
- Lee, Y. M.; Lee, J. Y.; Shim, H. T.; Lee, J. K.; Park, J.-K. *J. Electrochem. Soc.* **2007**, *154* (6), A515–A519.
- Jiang, T.; Zhang, S.; Qiu, X.; Zhu, W.; Chen, L. *Electrochem. Commun.* **2007**, *9*, 930–934.
- Leroy, S.; Blanchard, F.; Dedryvere, R.; Martinez, H.; Carre, B.; Lemordant, D.; Gonbeau, D. *Surf. Interface Anal.* **2005**, *37*, 773–781.

(18) Barsoukov, E.; Kim, J. H.; Kim, J. H.; Yoon, C. O.; Lee, H. *Solid State Ionics* **1999**, *116*, 249.

(19) Dollé, M.; Orsini, F.; Gozdz, A. S.; Tarascon, J.-M. *Electrochem. Soc.* **2001**, *148* (8), A851.

(20) Ho, C.; Raistrick, I. D.; Huggins, R. A. *J. Electrochem. Soc.* **1980**, *127* (2), 343–350.

(21) Wen, C. J.; Ho, C.; Boukamp, B. A.; Raistrick, I. D.; Weppner, W.; Huggins, R. A. *Int. Mater. Rev.* **1981**, *5*, 253–268.

(22) Boukamp, B. A. *Solid State Ionics* **1986**, *20*, 31–44.

(23) Barsoukov, E.; Kim, D. H.; Lee, H.-S.; Lee, H.; Yakovleva, M.; Gao, Y.; Engel, J. F. *Solid State Ionics* **2003**, *161*, 19–29.

(24) Limthongkul, P.; Jang, Y. I.; Dudney, N. J.; Chiang, Y. M.; Power, J. *Sources* **2003**, *119–121*, 604–609.

JP901594G